Advanced Materials Technologies

ADVANCED MATERIALS TECHNOLOGIES
www.advmattechnol.com

RESEARCH ARTICLE OPEN ACCESS

Rapid Room-Temperature Ethanol Sensing in Bi_2MoO_6/rGO Heterostructures: Weak Adsorption-Driven Charge Modulation

Sagarika Panda[1] | Savita Mehlawat[1] | Kwanghyeon Jo[2] | Neeraj Dhariwal[3] | Chang Woo Myung[2] | Mohd. Arif[4] | Sung Bum Kang[5] | Amit Sanger[1]

[1]Material Analysis and Research Laboratory, Department of Physics, Netaji Subhas University of Technology, New Delhi, India | [2]Department of Energy Science, Sungkyunkwan University, Suwon, Republic of Korea | [3]Graduate School of Integrated Science and Technology, Nagasaki University, Nagasaki, Japan | [4]Centre for Nanoscience and Nanotechnology, Faculty of Sciences, Jamia Millia Islamia, New Delhi, India | [5]Semiconductor Materials Components Equipment Technology Center, Electronics and Telecommunications Research Institute, Daejeon, Republic of Korea

Correspondence: Sung Bum Kang (kangsb@etri.re.kr) | Amit Sanger (amit.sanger@nsut.ac.in)

Received: 16 March 2026 | **Revised:** 21 June 2026 | **Accepted:** 23 June 2026

Keywords: Bi2MoO6/rGO heterostructure | ethanol detection | room-temperature gas sensor | weak adsorption kinetics

ABSTRACT

Chemiresistive sensors based on graphene derivatives and metal oxides continue to attract attention, yet achieving rapid and selective room-temperature detection remains challenging due to sluggish surface kinetics and limited understanding of interfacial interactions. Here, we report a Bi_2MoO_6/reduced graphene oxide (rGO) heterostructure synthesized via hydrothermal synthesis and integrated onto interdigitated electrodes via blade coating. The device delivers outstanding ethanol sensing at 27°C, exhibiting a ~16-fold enhancement over pristine Bi_2MoO_6 at 100 ppm, rapid 13/18 s response–recovery dynamics, a detection limit of 1.6 ppm, and excellent reproducibility and long-term stability. A portable prototype module incorporating this sensor further demonstrates reliable real-time ethanol monitoring, highlighting its practical applicability for environmental and breath analysis. To elucidate the origin of the unusual sensing behavior, we combine density functional theory (DFT) calculations with COMSOL-based kinetic modeling. Despite its lowest adsorption energy among the tested analytes, ethanol induces the largest conduction-band perturbation at the interface, whereas kinetic simulations reveal that weak adsorption accelerates adsorption–desorption turnover, thereby enabling frequent charge-transfer events within the sensing timescale. This cooperative interplay between weak binding and dynamic interfacial modulation explains the exceptional selectivity and ultrafast response. These results establish Bi_2MoO_6/rGO as a mechanism-guided platform for high-performance room-temperature gas sensing device development.

1 | Introduction

As humanity advances, industrialization speeds up, increasing the amount of volatile organic compounds (VOCs) released into the environment. Exposure to several VOCs can cause fatalities as well as major health harm [1, 2]. A common volatile organic compound, ethanol is widely used in a range of industries, including medicine, chemistry, food production, environmental monitoring, traffic safety, and cosmetics manufacturing [3, 4]. However, research has indicated that prolonged exposure to ethanol at levels below 25 parts per million can damage the human central nervous system, resulting in headaches [5]. Furthermore, ethanol will result in catastrophic losses in the case of an open flame because it is a volatile and combustible gas. Ethanol is volatile and explosive, and it is classified as a Class A hazardous product [1, 6]. Ethanol has an explosive range of 3.3%–19%. It may

be lit by electric sparks, electrostatic discharge, and human body fire, and its minimal ignition energy is about 0.63 Mj [7]. Thus, it is crucial to keep track of ethanol gas at low concentrations with high sensitivity and accuracy in order to safeguard public health and prevent safety incidents. Thus, real-time trace ethanol gas analysis has emerged as a successful strategy to prevent fire, poisoning, and other dangers [8]. Recent advancements of ethanol sensors that operate at room-temperature have demonstrated the potential for use in numerous domains. Based on their various operating principles, the gas sensors employed for detecting ethanol gas may be classified as electrochemical, thermoelectric, semiconductor, acoustic, and optical. Amongst, the MOS gas sensor has emerged as a hotspot for gas sensor research because of its easy manufacturing, affordability, mobility, and capacity to conduct online monitoring [9].

Reduced graphene oxide (rGO) is a 2D material with a honeycomb structure, known for its high electron transport efficiency, large surface area, photogenerated electron activity, and exceptional thermal and electrical properties [10, 11]. It also offers excellent carrier mobility and can be manufactured on a large scale. When combined with other materials, rGO is a perfect support material that may be used for a variety of purposes, including energy storage, photoconductive switching, bioimaging, and gas sensing [12, 13]. Regardless of orientation or adsorption sites, rGO has higher gas adsorption energy than graphene and promotes gas molecule adsorption. Because of this, rGO flakes have drawn a lot of attention as potentially useful parts for gas sensors [14].

Bi_2MoO_6, a well-known perovskite-type composite oxide with exceptional electrochemical characteristics, is a topic of great interest in several fields, including high-performance capacitors and photocatalysis [15]. Its structure consists of alternating $[Bi_2O_2]^{2+}$ layers and $[MoO_4]^{2-}$ octahedra, which create stable and open interlayer channels that are ideal for effective charge separation and transfer [4, 16]. Bi_2MoO_6, which has a bandgap between 2.6 and 2.8 eV, is thought to be a promising material for a number of uses. Its promise in visible light-driven self-cleaning surfaces, photoelectrochemical systems, luminescent materials, photocatalysis, and gas sensing technologies has garnered significant attention during the past few decades [17].

This work presents the hydrothermally generated Bi_2MoO_6/rGO material for ethanol sensing, which is its first use in gas sensor research. When compared to pure Bi_2MoO_6, the addition of rGO greatly improves ethanol selectivity, response/recovery times, and charge-transfer. Unlike conventional metal oxide sensors, which function at elevated temperatures, the Bi_2MoO_6/rGO composite demonstrates efficient ethanol detection at 27°C, making it energy-efficient and highly responsive.

2 | Experimental

2.1 | Preparation of Bi_2MoO_6

The hydrothermal process was used to synthesize Bi_2MoO_6. Initially, 1.214 g of sodium molybdate ($Na_2MoO_4.2H_2O$, Thomas Baker, minimum assay 98%) and 2.43 g of bismuth nitrate ($Bi(NO_3)_3.5H_2O$, Thomas Baker, minimum assay 98%) were blended with 7.3 mL of ethanediol and 3.64 mL of DI, and each was stirred individually for 30 min at 55°C. After that, they were both combined and stirred for about an hour at 55°C. After that, the mixture was autoclaved at 150°C for 15 h. The product was then centrifuged, cleaned with DI, and evaporated within the vacuum chamber for roughly 48 h to obtain Bi_2MoO_6.

2.2 | Preparation of Bi_2MoO_6/rGO

While 2 wt.% of rGO (Purchased from Techinstro) was being sonicated for 30 min, 2 g of Bi_2MoO_6 were combined with DI and thoroughly agitated. Following the mixing of both, the mixture was swirled for 1 h. After that, the prepared solution was heated in a vacuum chamber for roughly 24 h in order to create the Bi_2MoO_6/rGO composite. Figure S1 depicts the synthesis process.

2.3 | Gas Sensing Setup

A precise experimental design adds important knowledge to the field of gas sensing. The sensing configuration employed in this investigation is shown in Figure S2. A sturdy design for useful and precise measurement is part of the setup. The highly pure gas cylinders of 100 ppm (Ethanol, NO_2, NH_3, Acetone, Methanol, TEA, petroleum) were taken from Sigma Gases, India. The setup used for the experiment consists of a 3 mL gas detection chamber where a regulated volume of ethanol is purged using conventional instruments and accurate measurements to track the gas level. Two Mass Flow Controllers (MFCs, MF-3000) were used for ethanol gas (100 ppm) and zero air in order to balance the concentration of gases. The resulting mixture was then placed in a gas sensor chamber with the appropriate concentration of gas. Additionally, a gas flow capacity of 100 SCCM was established. Furthermore, an IDE (interdigitated electrodes) with cutting-edge sensing components was positioned in the chamber to monitor as well as assess the gas interactions. A Keithley 2450 source meter is part of the gas sensing system, which allows for the real-time monitoring of sensor response to changes in ethanol levels. Every measurement is carried out in a controlled setting with a temperature of 27°C. The sensor response for reducing gas (like ethanol) and for oxidizing gas measurement is obtained by using Equations (1) and (2), respectively [18, 19]:

$$Response\,(Reducinggas) = \frac{R_a}{R_g} \tag{1}$$

$$Response\,(Oxidisinggas) = \frac{R_g}{R_a} \tag{2}$$

where, R_a, R_g represents initial resistance and the resistance after gas exposure of the sensor.

2.4 | Fabrication of Sensor

The sensor was eventually fabricated using the synthesized material. Distilled water was used to create a slurry using Bi_2MoO_6/rGO nanoparticles. Applying the blade coating

approach, the obtained slurry was then placed over a gold IDE. The deposited film was then employed for ethanol detection after being dried for 2 h at 70°C using a vacuum chamber.

The fabricated sensor was evaluated for breath detection by exposing it to human exhaled breath. The exhaled-breath measurement was conducted with a volunteer participant who provided informed consent prior to the experiment.

2.5 | Density Functional Theory Calculations

In this study, density functional theory (DFT) calculations were performed using the Vienna Ab initio Simulation Package (VASP) [20]. We used the Projector Augmented-Wave (PAW) method and Perdew–Burke–Ernzerhof (PBE) functional [21]. To accurately consider long-range van der Waals interactions, van der Waals corrections were applied using the DFT-D4 method [22]. The plane wave energy cutoff was set to 600 eV, and a (1 × 1 × 1) k-point grid was applied for Brillouin zone integration. Optimization of atomic geometry was performed until each force was less than 0.02 eV/Å, and the energy convergence criterion was set to 10^{-7} or 10^{-8} eV, depending on the system.

2.6 | COMSOL

Numerical simulations were performed using COMSOL Multiphysics (version 6.1) to investigate the adsorption–desorption kinetics and resistance response of the Bi_2MoO_6/rGO heterostructure. The Chemical Reaction Engineering Module was employed with the *Transport of Diluted Species* physics interface, coupled to a user-defined surface reaction model to capture Langmuir-type adsorption behavior.

2.6.1 | Surface Coverage θ(t)

Surface coverage θ(t) of ethanol and acetone molecules on the Bi_2MoO_6/rGO interface using a classical Langmuir adsorption–desorption framework by COMSOL. In this model, the fractional surface coverage is described by

$$\theta(t) = \frac{K_{ads}C}{K_{ads} + K_{des}} [1 - \exp(-(K_{ads}C + K_{des})\, t] \quad (3)$$

where K_{ads} and K_{des} represent the adsorption and desorption rate constants, respectively, and C is the analyte concentration. The equilibrium coverage is therefore determined by

$$\theta_{eq} = \frac{K_{ads}C}{K_{ads}C + K_{des}} \quad (4)$$

2.6.2 | Geometry and Domain

The simulation domain was constructed as a 2D rectangular cross-section (length: 10 µm, thickness: 0.5 µm), representing the rGO sensing layer exposed to the analyte gas phase. The gas reservoir was modeled as a 10 µm × 5 µm rectangular domain above the sensing layer. The bottom boundary of the rGO domain was fixed as impermeable to simulate the underlying Bi_2MoO_6 support.

2.6.3 | Governing Equations

The gas-phase transport was described by the diffusion equation:

$$\frac{\partial C}{\partial t} = D\nabla^2 C \quad (5)$$

where C is the analyte concentration (mol·m^{-3}), and D is the diffusion coefficient (set to 1.5×10^{-5} m^2·s^{-1} for ethanol and 1.3×10^{-5} m^2·s^{-1} for methanol, consistent with literature values).

At the gas-sensor interface, surface coverage θ(t) was defined by the Langmuir adsorption–desorption equation:

$$\frac{d\theta}{dt} = K_{ads}C\,(1 - \theta) - K_{des}\theta \quad (6)$$

2.6.4 | Parameterization

The adsorption and desorption constants were parameterized based on DFT adsorption energies. For ethanol (−0.402 eV), a relatively fast adsorption ($K_{ads} = 8.0 \times 10^{-4}$ m^3·mol^{-1}·s^{-1}) and fast desorption ($K_{des} = 5.0 \times 10^{-3}$ s^{-1}) were chosen to reflect weak binding. For methanol (−0.485 eV), slower adsorption ($K_{ads} = 3.0 \times 10^{-4}$ m^3·mol^{-1}·s^{-1}) and slower desorption ($K_{des} = 1.5 \times 10^{-3}$ s^{-1}) were selected to reflect stronger binding and reduced turnover. The inlet concentration was fixed at 50 ppm (2.05×10^{-3} mol·m^{-3}) for both analytes.

2.6.5 | Boundary Conditions and Solver Settings

- Top boundary: constant analyte concentration ($C = C_0$).
- Side boundaries: no flux ($\partial C/\partial n = 0$).
- Bottom boundary: impermeable (no analyte penetration into Bi_2MoO_6).
- Gas-rGO interface: coupled adsorption–desorption boundary condition described above.

The simulations were solved using a time-dependent solver (BDF scheme) with a maximum time step of 0.1 s. Total simulation time was 100 s to capture both the adsorption (response) and desorption (recovery) phases.

2.6.6 | Sensor Response Mapping

The normalized resistance change was calculated as:

$$\frac{\Delta R}{R_0}(t) \propto \eta.\theta(t) \quad (7)$$

where η is the charge-transfer efficiency factor determined from DFT-calculated CBM shifts (η_ethanol = 1.5, η_methanol = 0.8).

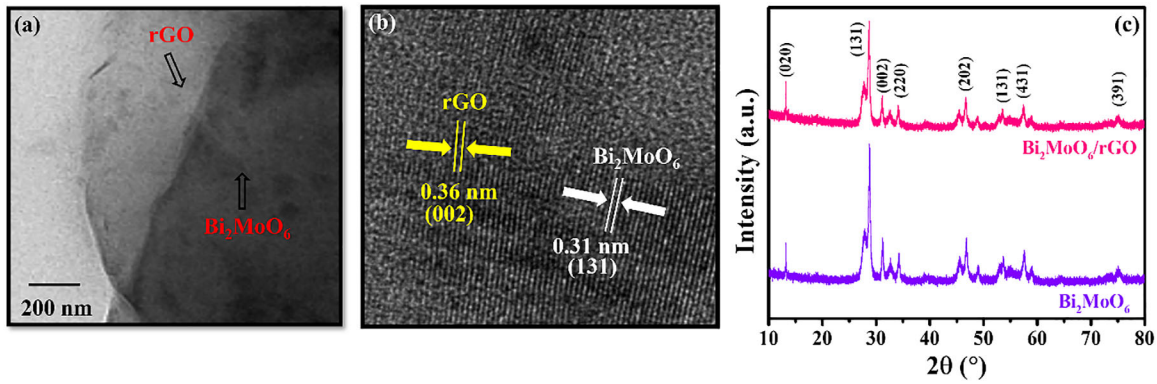

FIGURE 1 | (a) HRTEM image, (b) d-spacing of Bi_2MoO_6/rGO, (c) XRD pattern of Bi_2MoO_6 and Bi_2MoO_6/rGO.

3 | Results and Discussion

3.1 | Structural and Morphological Investigation

To learn further regarding the crystalline and phase development of the manufactured materials, X-ray diffraction (XRD) was carried out to determine the chemical structure of Bi_2MoO_6 and Bi_2MoO_6/rGO employing an X-ray diffractometer (using CuKα radiation), as illustrated in Figure 1c. Bi_2MoO_6's prominent diffraction peak indicates that it is a highly crystalline substance. The peaks corresponding to the (020), (131), (002), (220), (202), (113), (431), and (391) match with the orthorhombic phase of Bi_2MoO_6 (Jcpds number: 01-072-1524) [23, 24]. As rGO has low crystallinity, no authentic peaks were observed in the XRD pattern; also, the lower concentration of rGO doesn't influence the orientation of Bi_2MoO_6 [25].

FESEM has been employed to validate the surface morphology of bare Bi_2MoO_6 and Bi_2MoO_6/rGO as represented in Figure S3. From Figure S3a, it has been clearly observed that Bi_2MoO_6 exhibits an agglomerated 3D nano-spherical-like structure corresponding to the Orthorhombic Crystal system. When rGO has been introduced, non-uniform folded nanosheets have been observed between the Bi_2MoO_6 nanosphere [26, 27], which can be depicted from Figure S3b. Additionally, Energy Dispersive X-ray (EDX) spectroscopy was performed to monitor the elemental composition and mapping over the scanned regions. Figure S3c presents the EDX spectrum of bare Bi_2MoO_6, revealing elemental concentrations of 24.23 wt.% oxygen (O), 21.55 wt.% molybdenum (Mo), and 54.22 wt.% bismuth (Bi). In contrast, Figure S3d reveals the EDX spectrum of the Bi_2MoO_6/rGO composite, indicating the presence of 19.13 wt.% carbon (C), 24.46 wt.% O, 16.19 wt.% Mo, and 40.22 wt.% Bi. Furthermore, the figure includes the combined electron image along with color-coded elemental maps, clearly illustrating the distribution of individual elements in both Bi_2MoO_6 and Bi_2MoO_6/rGO samples.

Bi_2MoO_6/rGO heterostructure was thoroughly analyzed for its structural and morphological characteristics using a high-resolution transmission electron microscope (HR-TEM). The HRTEM image clearly shows the interface between Bi_2MoO_6 and rGO, demonstrating that Bi_2MoO_6 is loaded onto rGO sheet to produce a heterostructure (Figure 1a). The sensor's efficacy is improved by this interfacial heterojunction, leading to more convenient for charges to transit through the heterojunction. The characteristic lattice fringes linked to Bi_2MoO_6/rGO heterostructures is illustrated in Figure 1b. According to this, the d-spacing of 0.31 and 0.36 nm denote (131) of Bi_2MoO_6 [28] and (002) of rGO [29], respectively, and it is also prominently illustrated in the inset of Figure 1b.

XPS examinations were conducted to have a better understanding of the material's composition and valence state. The XPS of Bi_2MoO_6 and Bi_2MoO_6/rGO, respectively, together with their peak deconvolutions, are displayed in Figure 2. The spectra of every element, including Bi, Mo, O, and C, are displayed in Figure 2a,e. The Bi 4f spectra of bare Bi_2MoO_6, shown in Figure 2b, display characteristic binding energies corresponding to Bi^{3+}, specifically Bi $4f_{7/2}$ and Bi $4f_{5/2}$. Additional peaks are observed at 159.02, 160.05, 164.31, and 165.41 eV. In comparison, the Bi 4f spectrum of the Bi_2MoO_6/rGO composite (Figure 2f) shows shifted peaks at 158.57, 159.07, 163.96, and 165.11 eV. This shift indicates electron transfer to the surface, attributed to the formation of $Bi^{(3-x)+}$ [30, 31]species due to an increase in oxygen vacancies around Bi^{3+} sites during the incorporation of rGO. Gas-sensing efficiency is increased when $Bi^{(3-x)+}$ is present because it inhibits electron–hole recombination. Mo $3d_{5/2}$ and Mo $3d_{3/2}$ states of Mo^{6+} are represented by peaks at 231.77, 232.92, 235.05, and 236.12 eV in the Mo 3d spectra for Bi_2MoO_6 (Figure 2c) [32]. These peaks are slightly displaced at 231.72, 232.92, 234.92, and 236.15 eV in the Bi_2MoO_6/rGO composite (Figure 2h), indicating interactions between Mo and rGO. Three peaks can be seen in the O 1s spectra of pure Bi_2MoO_6 (Figure 2d), with lattice oxygen at 531.01 eV, vacancy oxygen at 532.09 eV, and chemisorbed oxygen at 533.41 eV. The performance of gas sensing is greatly improved by these vacancies. Additionally, the presence of carbon species from rGO is confirmed by the two conspicuous peaks in the C 1s spectra of Bi_2MoO_6/rGO (Figure 2i) at 284.86 and 286.24 eV [33]. All things considered, the observed changes in binding energies for every element point to the development of heterojunction interfaces between rGO and Bi_2MoO_6. The composite's ability to detect ethanol gas is greatly improved by this heterostructure, which promotes electron transport from rGO to Bi_2MoO_6, increasing electron density and carrier concentration.

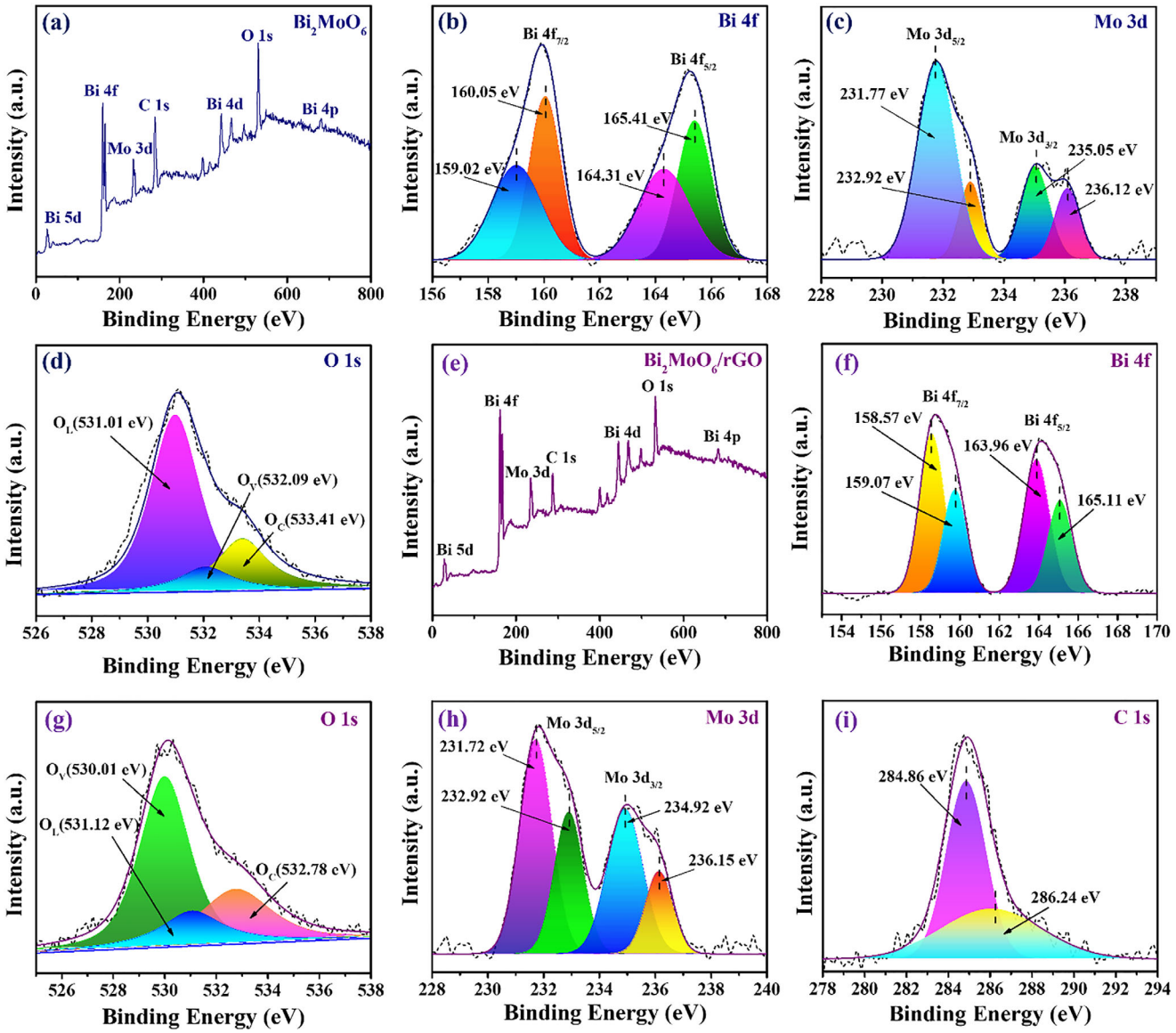

FIGURE 2 | (a,e) Full XPS and high-resolution spectrum of (b,f) Bi 4f, (d,g) O 1s, (c,h) Mo 3d, and (i) C1s of Bi_2MoO_6 & Bi_2MoO_6/rGO, respectively.

3.2 | Gas Sensing Study

The manufactured sensor's performance in the presence of ethanol gas at a temperature of 27°C was evaluated. As mentioned in the previous section, the composite of Bi_2MoO_6/rGO exhibits superior sensing performance despite bare Bi_2MoO_6 (Figure 3b,c). This is because of its higher porosity and excellent selectivity. Rapid electron transport and gas adsorption are made possible by pristine rGO's huge specific surface area, plentiful adsorption sites, and highly conductive network. However, because there are fewer active catalytic sites and less charge carrier concentration modification when exposed to ethanol, isolated rGO has a relatively reduced sensing response and selectivity [34, 35]. On the other hand, through synergistic effects such as enhanced charge separation, efficient interfacial electron transfer, increased active adsorption sites, and heterointerface-induced modulation of carrier transport, the formation of the Bi_2MoO_6/rGO heterostructure greatly improves the sensing performance. In comparison to pure rGO, Bi_2MoO_6 alone, the close interfacial contact between Bi_2MoO_6 and rGO facilitates faster charge-transfer kinetics and stronger interaction with ethanol molecules, leading to higher selectivity, enhanced response, and faster response/recovery characteristics. The manufactured sensor exhibits n-type sensor behavior while contacted with ethanol; its resistance capacity drops rapidly and returns to its starting state when reintroduced to air.

When ethanol (reducing gas) is present, the active chemisorbed oxygen combines with the ethanol molecule and returns electrons to the surface of the nanoparticle's conduction band. The resistance of the sensor will consequently decrease as the carrier concentration increases [36, 37]. Initially, for the pristine Bi_2MoO_6 and rGO, the responses to ethanol gas at 100 ppm were found to be 14.2 (R_a/R_g = 14.2), 8.7, respectively (depicted in Figure 3a,b), and for Bi_2MoO_6/rGO, the response dynamically increases to 233.7 (Figure 3c). Additionally, the sensor provides a fast response time (τ_{res} = 13 s) and a quick recovery time (τ_{rec} = 18 s), which is significantly improved compared to pure

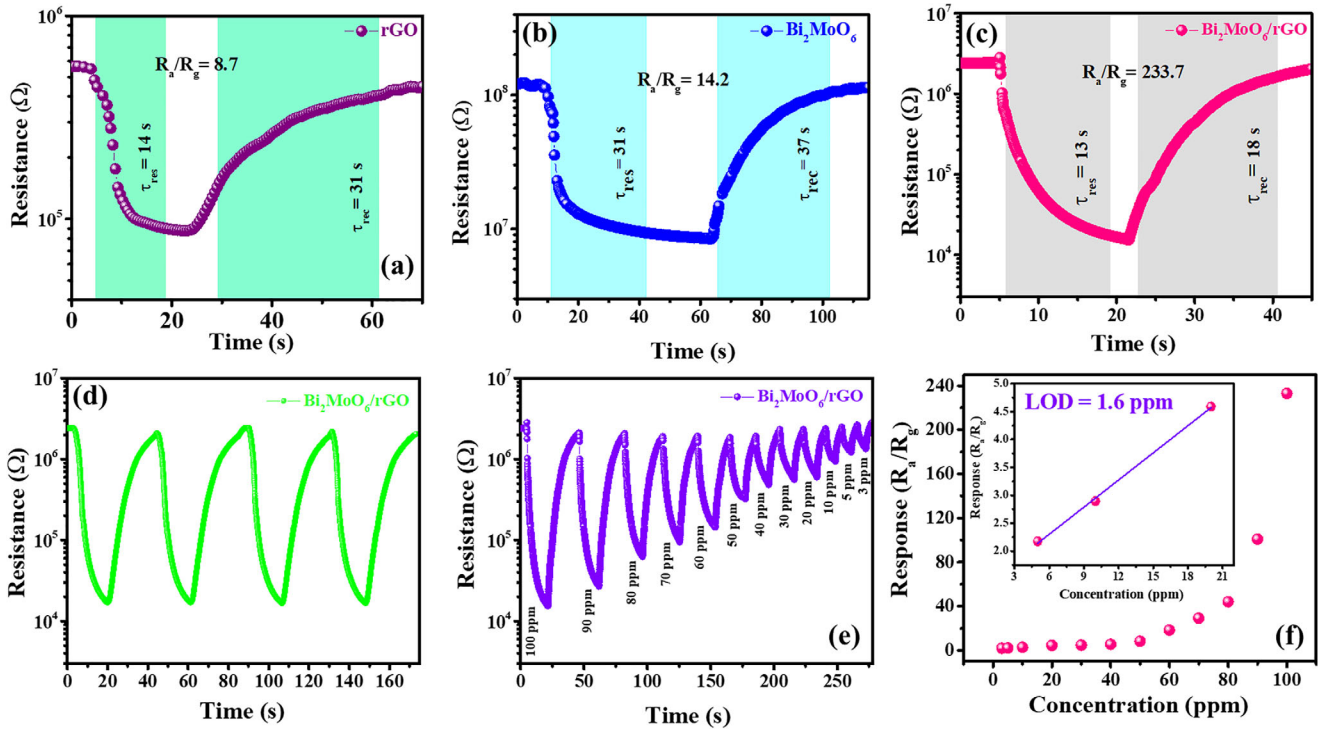

FIGURE 3 | (a–c) Response and recovery time of rGO, Bi_2MoO_6, Bi_2MoO_6/rGO, respectively at 100 ppm, (d) repeatability of the Bi_2MoO_6/rGO sensor at 100 ppm of ethanol gas (e) performance of Bi_2MoO_6/rGO based sensor at different ppm levels of ethanol gas; (f) LOD of Bi_2MoO_6/rGO sensor.

Bi_2MoO_6 (τ_{res} = 31 s, τ_{rec} = 37 s) and rGO (τ_{res} = 14 s, τ_{rec} = 31 s). As repeatability is one of the major factors of any sensor, the Bi_2MoO_6/rGO sensor was tested repeatedly in 100 ppm of ethanol gas, which shows excellent stability and recyclability (Figure 3d). The fabricated sensor was tested up to 100 to 3 ppm experimentally by varying the ethanol concentration as depicted in Figure 3e. The developed sensor exhibits a low LOD (Limit of detection), specifically 1.6 ppm (Figure 3f), with curve fitting of the sensor response to concentration yielding an R^2 value of 0.99. The LOD value was derived from the fitting/extrapolation of the concentration-response calibration curve. A linear fitting model was used to fit the sensor response values measured at various ethanol concentrations, and the standard relation was used to get the LOD:

$$LOD = \frac{3\sigma}{S} \tag{8}$$

where S is the slope of the linear fitted calibration curve, and σ is the standard deviation.

The selectivity of any sensor is its salient feature, which is determined by the sensor's behavior with gas interaction. The fabricated sensor was pursued into different gas atmospheres, including NH_3, acetone, triethylamine (TEA), methanol, NO_2, and petroleum at 100 ppm. In comparison to other gases, the sensor responded best to ethanol gas as shown in Figure 4a. First, ethanol has a low diffusion rate, which suggests the ethanol gas may be easily absorbed on the surface of Bi_2MoO_6/rGO material. In addition, ethanol has a longer alkyl chain length, so throughout the period, the adsorbed oxygen atom encounters alcohols with a higher alkyl chain length, the carrier concentration will rise [38]. Finally, the activation energy of ethanol is lower than that of other gases [39]. Figure 4b displays a graph that illustrates how humidity affects sensor response under 0%–90% relative humidity range. A humidity monitor was used to measure the artificially produced humid atmosphere in the gas sensing chamber. It is evident from the study's findings that sensor sensitivity progressively decreases with increasing humidity. In a highly humid environment, adsorption of water molecules reduces the chemisorption of oxygen species over material surfaces, which in turn reduces sensor response. Furthermore, the adsorption of ethanol molecules is inhibited by excessive humidity, which reduces the sensor's responsiveness [40, 41]. Additionally, as shown in Figure 4c, long-term stability tests were carried out using ethanol gas at 100 ppm. Following 45 days of testing, the findings of the experiment indicate that the Bi_2MoO_6/rGO sensor had an average response of 234.6, showing minor response modifications over time and offering compelling proof for its exceptional durability. Again, to confirm the repeatability and dependability of the sensor performance, five independently constructed Bi_2MoO_6/rGO sensor devices were used to assess the reported sensing response of 233.7 toward 100 ppm ethanol as well as the fast response/recovery characteristics. The relative standard deviation (RSD) of the sensor response was 0.73% (Figure 4d), indicating strong fabrication consistency and excellent reproducibility. A comparative study of different materials for Ethanol sensing is given in Table 1.

Figure 5 integrates the DFT calculations and COMSOL kinetic simulations to clarify the sensing behavior of the Bi_2MoO_6/rGO heterostructure. The atomistic model (Figure 5a) was constructed by combining oxygen-functionalized rGO (~5 at.%) with orthorhombic Bi_2MoO_6, applying a moderate biaxial strain (<

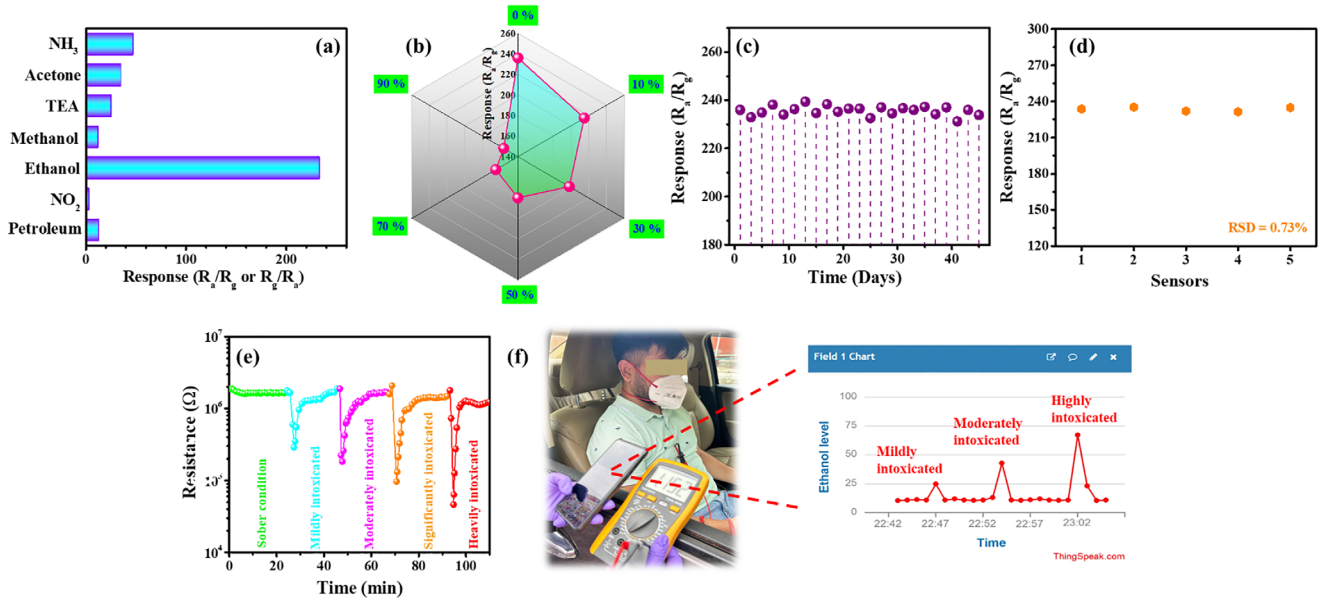

FIGURE 4 | (a) Selectivity of the Bi_2MoO_6/rGO based sensor, (b,c) response of Bi_2MoO_6/rGO sensor as a function of relative humidity and days at 100 ppm of ethanol gas, (d) Response for five reproducible Bi_2MoO_6/rGO sensors, (e) Ethanol gas sensor in breath alcohol detection, (f) Practical application along with IoT based signal transmission.

TABLE 1 | Comparative study of different materials for Ethanol sensing.

S. No.	Materials	Gas concentration	Operating temperature (°C)	Res/Rec (s)	Response (R_o/R_g)	Refs.
1	Bi_2MoO_6 Nanosheets	100 ppm	275	—	5.55	[53]
2	Bi_2WO_6	50 ppm	290	7/14	60.8	[54]
3	Bi-doped rGO/Co_3O_4	100 ppm	120	89/75	150	[55]
4	α-$Bi_2Mo_3O_{12}$/Co_3O_4	100 ppm	170	—	30.25	[56]
5	Zn_2SnO_4/rGO	100 ppm	275	11/18	38	[57]
6	CuO/rGO nanosheets	100 ppm	175	328/446	10.54	[58]
7	$ZnFe_2O_4$NSs/rGO	100 ppm	210	14/37	41.5	[59]
8	Bi_2MoO_6/rGO	100 ppm	27	13/18	233.7	This work

4%) to achieve lattice commensurability. The projected density of states of the pristine interface (Figure 5b) shows nearly flat band alignment with only ~1 meV offset at the CBM, confirming that the heterointerface itself does not induce electronic perturbation in the absence of analytes. Calculated adsorption energies (Figure 5c) follow the order acetone (−0.512 eV) > methanol (−0.485 eV) > ethanol (−0.402 eV), highlighting that ethanol interacts most weakly with the rGO surface. Nevertheless, the CBM shifts induced by adsorption (Figure 5d,e,f) show the opposite trend: ethanol produces the largest negative ΔCBM (−12.3 meV), while methanol induces a smaller shift (−9.0 meV), and acetone produces a positive shift (+15.9 meV). Unlike methanol and ethanol, which both act as electron donors to the rGO conduction network, acetone withdraws electrons and drives the CBM upward, thereby suppressing conduction and weakening the resistance response despite its stronger binding. It should be noted that a lower adsorption energy does not necessarily imply a weaker chemiresistive response, particularly under room-temperature dynamic sensing conditions. In chemiresistive gas sensors, the response and recovery characteristics are strongly affected not only by equilibrium adsorption strength but also by adsorption–desorption kinetics and surface charge-transfer-induced conductance modulation [42–44]. In this context, weakly adsorbed ethanol can undergo rapid adsorption–desorption turnover, enabling frequent charge-transfer events within the sensing timescale. Moreover, despite its weak binding, ethanol induces the most pronounced conduction-band perturbation at the Bi_2MoO_6/rGO interface, as revealed by the DFT calculations. Therefore, the exceptional ethanol response arises from the combined effect of fast adsorption–desorption kinetics and large interfacial electronic modulation, rather than from adsorption strength alone [45–48].

To further connect adsorption energetics with device-level sensing behavior, COMSOL simulations were carried out using a Langmuir adsorption–desorption framework. The time evolution of surface coverage $\theta(t)$ for methanol and ethanol is shown in Figure 5g. Because of its poor binding and quick desorption

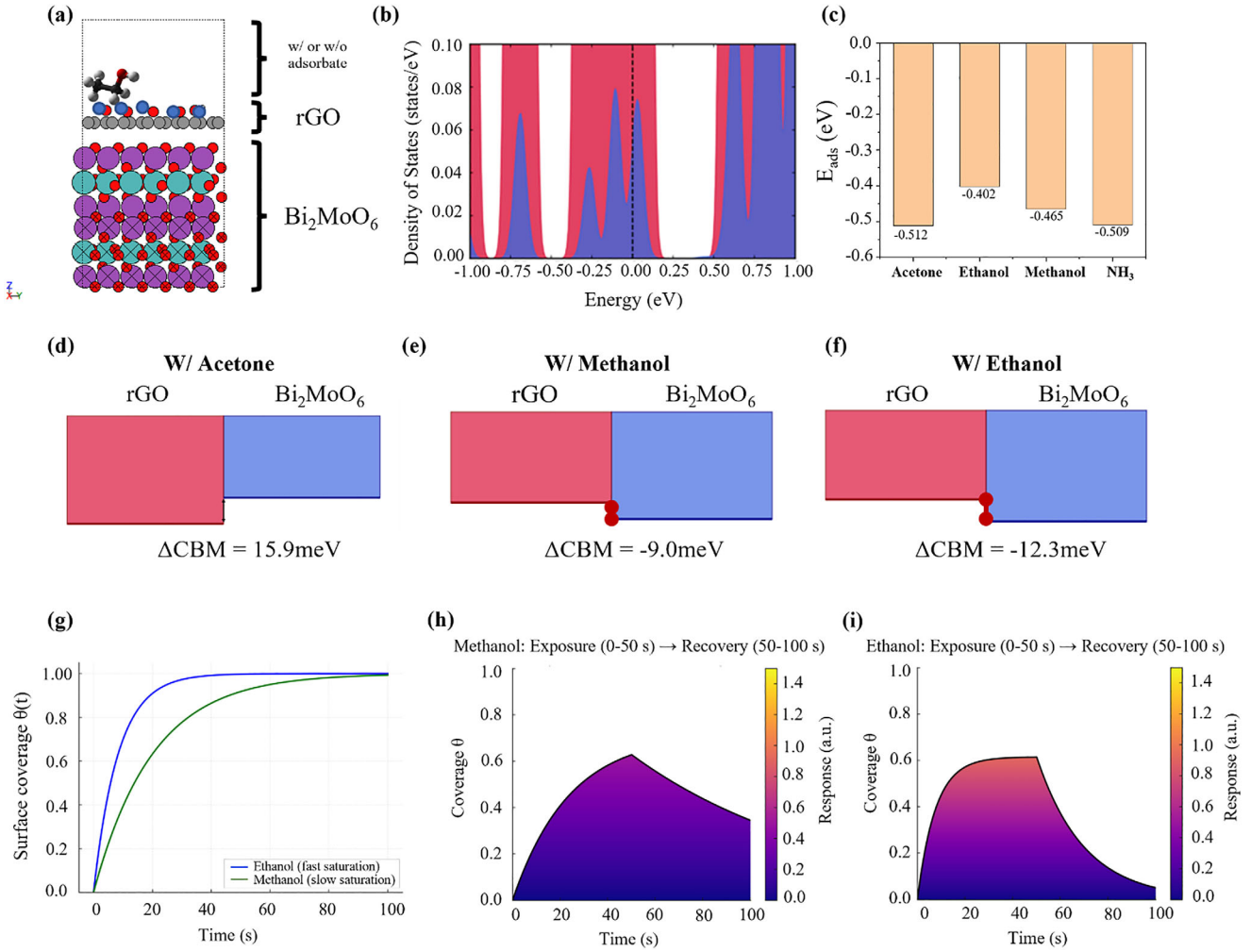

FIGURE 5 | (a) Computational model of the Bi_2MoO_6/rGO heterostructure used in DFT simulations. The rGO lattice (oxygen content ≈5 at.%) was strained to achieve commensurate matching with orthorhombic Bi_2MoO_6. (b) Projected density of states (PDOS) of the pristine interface shows nearly flat CBM alignment (~1 meV), indicating minimal electronic perturbation in the absence of analytes. (c) Calculated adsorption energies of representative analytes, showing strongest binding for acetone (−0.512 eV) and weakest binding for ethanol (−0.402 eV). (d–f) CBM shifts induced by gas adsorption: ethanol produces the largest negative shift (−12.3 meV), methanol induces a smaller negative shift (−9.0 meV), while acetone drives a positive shift (+15.9 meV), consistent with its electron-withdrawing nature. (g) Comparison of adsorption–desorption kinetics obtained from COMSOL simulations, where ethanol rapidly reaches saturation while methanol approaches equilibrium more slowly. (h,i) Heatmap representations of simulated response intensity ($\theta \times \eta$) during gas exposure (0–50 s) and recovery (50–100 s). The black line indicates the actual surface coverage trajectory $\theta(t)$ obtained from Langmuir adsorption–desorption kinetics. For methanol (h), stronger binding results in a slower approach to equilibrium during exposure and more gradual desorption during recovery, yielding a weaker but more persistent response. In contrast, ethanol (i) exhibits weak binding and a high desorption rate, leading to rapid saturation and fast decay, which produces a stronger but more transient response. White regions correspond to inaccessible states beyond the instantaneous coverage $\theta(t)$.

kinetics, ethanol quickly saturates to complete coverage in tens of seconds, but methanol takes a significantly longer time to reach equilibrium because of its stronger surface interaction. This kinetic difference explains how ethanol molecules can dynamically go through several cycles of adsorption and desorption within the sensing period, increasing the frequency of charge-transfer events.

The dynamic adsorption–desorption simulations shed more light on how the Bi_2MoO_6/rGO heterostructure's sensing response is simultaneously determined by binding strength and charge-transfer efficiency. The simulated heatmap for methanol is shown in Figure 5h. Because of its lower desorption rate and stronger binding energy, the surface coverage $\theta(t)$ increases gradually across the exposure time (0–50 s). Methanol slowly desorbs even after the gas source is cut off, which slows down the recovery process. As a result of limited carrier modulation and slow kinetics, the effective response intensity is still comparatively weak but more persistent.

Ethanol, on the other hand, shows a completely different dynamic behavior (Figure 5i). Rapid saturation of accessible surface sites during exposure is made possible by its lower adsorption energy and higher desorption rate, which are followed by rapid desorption after the gas flow is stopped (50–100 s). In line with the experimentally observed steep rise and quick recovery in

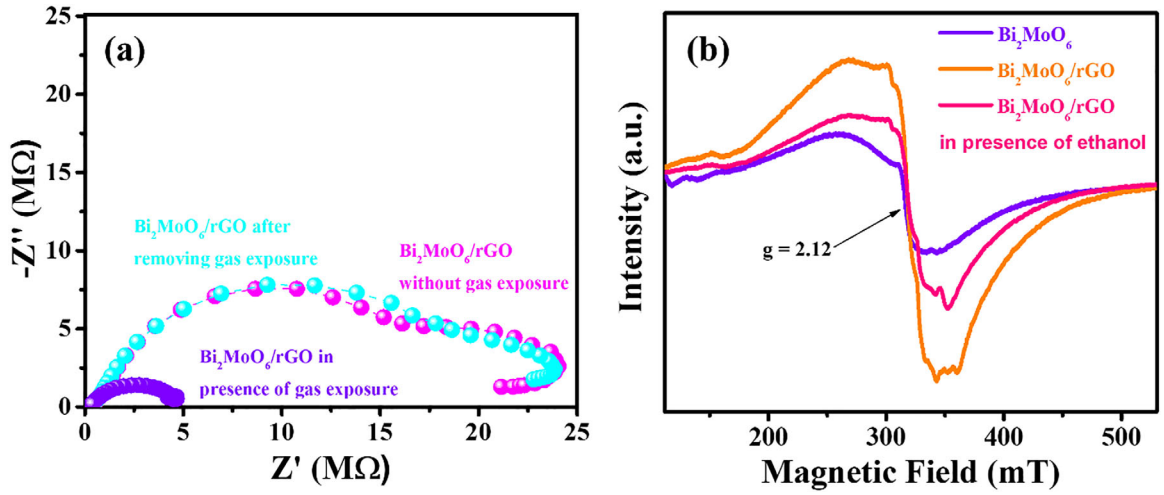

FIGURE 6 | Comparative (a) EIS and (b) EPR study of the sensor.

resistance transients, this dynamic turnover generates a stronger but more fleeting reaction. Crucially, these heatmaps highlight that the sensing signal results from the interaction of adsorption kinetics and charge-transfer efficiency rather than being solely controlled by equilibrium surface coverage. Despite its weaker binding, ethanol frequently interacts with the rGO conduction network, effectively donating charge during each adsorption–desorption cycle, whereas methanol stabilizes on the surface with minimal disturbance of the conduction band. This explains why ethanol produces the largest resistance response experimentally, even though its static binding energy is the smallest among the studied analytes.

At room-temperature, the chemisorption of oxygen into O^- species is energetically suppressed. Therefore, conventional sensing pathways dominated by oxygen redox reactions are negligible under low-temperature, low-ppm conditions. Instead, the response is governed by direct interactions between the analyte and the sensing surface. For ethanol, weak binding facilitates high surface mobility and rapid adsorption–desorption dynamics [49, 50]. Ethanol molecules can transiently occupy multiple sp^2 domains and shallow states, enabling efficient charge-transfer despite weaker static adsorption [51]. This dynamic sampling mechanism amplifies electron donation into the rGO-Bi_2MoO_6 system, leading to the largest experimental resistance modulation, in line with prior reports on low-temperature rGO-based sensors.

In order to acquire a better understanding of the electrical conductivity of Bi_2MoO_6/rGO sample in the absence and presence of ethanol gas, an impedance study was conducted. The EIS (Electrochemical Impedance Spectroscopy) measurements were performed using a Keysight impedance analyzer by applying a small AC voltage perturbation over a broad frequency range (20 Hz–10 MHz) under ambient conditions. The impedance response of the sensing material was recorded both in the absence and in the presence of 100 ppm ethanol gas to evaluate the effect of gas exposure on the electrical transport properties of the sensor. The real and imaginary components of impedance obtained from the measurements were used to construct Nyquist plots, which were further analyzed to investigate the charge-transfer resistance, interfacial electron transport behavior, and gas-induced modulation of carrier dynamics in the sensing material. It is found that the diameter of the arc radius of Bi_2MoO_6/rGO in presence of ethanol is smaller than that in the absence of ethanol gas (Figure 6a), suggesting less resistance, because the induced oxygen vacancies function as n-type carrier dopants to enhance the conductivity [52]. Additionally, the two curves that exhibit a comparable structure when the ethanol gas is absent and after it is removed reflect a favorable recovery state. Figure 6b provides the EPR spectra of Bi_2MoO_6, Bi_2MoO_6/rGO, and Bi_2MoO_6/rGO in the presence of ethanol gas. Samples display a Lorentz line (g = 2.12) as illustrated in Figure 6b. Here, the signal intensity of the Bi_2MoO_6/rGO composite is significantly higher than that of pure Bi_2MoO_6, which can be attributed to the interaction among carbon-inherited spin species, π-electrons in condensed sp^2 domains of rGO sheets. In presence of ethanol gas, the intensity is low due to the transfer of electrons into the vacancies.

3.3 | Application

Because of their quick reaction time, selectivity, and versatility, ethanol sensors have garnered a lot of attention. These include industrial safety systems where ethanol vapor detection is crucial for preventing fire hazards, the food and beverage industry for managing fermentation processes, the automotive industry for monitoring ethanol-blended fuels, and environmental monitoring for identifying volatile organic compounds. Ethanol sensors are also crucial for healthcare and law enforcement, especially in breathalyzers that are used for non-invasive alcohol detection and assessment of drunk driving.

Breath alcohol detection is the subject of the current study since it is crucial for preserving public safety and may find utility in personal alcohol monitoring devices. This led to the development and evaluation of the first ethanol sensor based on a Bi_2MoO_6/rGO nanocomposite. The sensor showed good selectivity, high sensitivity, and fast response-recovery behavior at 27°C. To mimic the real intoxication profiles shown in Figure 4e, we applied controlled ethanol exposures spanning sober to heavily

intoxicated states under saturated relative humidity conditions characteristic of human breath. As a result of the analysis and mapping of these levels onto a five-stage drunkenness scale, the sensor can be used to estimate levels of intoxication in addition to detection. The developed sensing system was tested in a controlled environment simulating alcoholic beverage exposure to evaluate its selectivity toward ethanol. Real-time detection results were displayed on a mobile interface (Thingspeak), as illustrated in Figure 4f. The results demonstrate the strong potential of Bi_2MoO_6/rGO-based sensors for integration into breathalyzers and smart alcohol detection systems.

4 | Conclusion

When rGO is used instead of pure Bi_2MoO_6, it greatly improves ethanol selectivity, decreases response/recovery times, and increases charge transport. Because the Bi_2MoO_6/rGO composite exhibits effective ethanol detection at 27°C, it is both extremely sensitive and energy-efficient in contrast to traditional metal oxide sensors that function at high temperatures. The sensor has a remarkable 16-times sensing response at approximately 100 ppm. It showed an 18 s recovery time, a 13 s reaction time, and a 1.6 ppm detection limit. The interaction between ethanol and Bi_2MoO_6/rGO nanocomposites was analyzed using DFT and COMSOL. These features are crucial for practical environmental monitoring and industrial safety applications since the sensor can successfully distinguish ethanol vapor from other interfering gases. The sensor's long-term stability and repeatability have already been verified, making it an excellent choice for trustworthy ethanol gas detection. The results demonstrate how well-suited Bi_2MoO_6/rGO based sensors are for integration into breathalyzers and intelligent alcohol detection systems. The sensor was also used to detect alcohol in breath.

Acknowledgements

This work was supported by the internal research fund of Electronics and Telecommunications Research Institute [26UC1100]. This research was also supported by the National Research Foundation of Korea (NRF) funded by the Korean government (Ministry of Science and ICT(MSIT)) (RS-2022-NR072058). We are grateful for the computational support from the Korea Institute of Science and Technology Information (KISTI) for the Nurion cluster (KSC-2025-CRE-0161, KSC-2025-CRE-0286, KSC-2025-CRE-0316, KSC-2025-CHA-0020) and Neuron cluster (KSC-2025-CRE-0093, KSC-2025-CRE-0122, KSC-2025-CRE-0164, KSC-2025-CRE-0341). Computational work for this research was partially performed on the Olaf supercomputer supported by IBS Research Solution Center and GPU cluster supported by Ministry of Science and ICT (MSIT) and the National IT Industry Promotion Agency (NIPA).

Conflicts of Interest

The authors declare no conflicts of interest.

Data Availability Statement

The data that support the findings of this study are available from the corresponding author upon reasonable request.

References

1. L. T. Nhiem, J. Mao, Q. T. Hoai Ta, and S. Seo, "Highly Selective Ethanol Gas Sensor Based on CdS/$Ti_3C_2T_X$ MXene Composites," *Nanoscale Advances* 7 (2025): 1452–1463, https://doi.org/10.1039/D4NA00927D.

2. C. Ban, X. Min, J. Xu, et al., "An Artificial Olfactory Memory System for Monitoring and Recording of Volatile Organic Compounds," *Advanced Materials Technologies* 6 (2021): 2100366, https://doi.org/10.1002/admt.202100366.

3. A. Umar, A. A. Ibrahim, U. T. Nakate, et al., "Fabrication and Characterization of CuO Nanoplates Based Sensor Device for Ethanol Gas Sensing Application," *Chemical Physics Letters* 763 (2021): 138204, https://doi.org/10.1016/j.cplett.2020.138204.

4. T. Han, J. Yang, R. Miao, et al., "Direct Distinguishing of Methanol over Ethanol with a Nanofilm-Based Fluorescent Sensor," *Advanced Materials Technologies* 6 (2021): 2000933, https://doi.org/10.1002/admt.202000933.

5. B. Jiang, T. Zhou, L. Zhang, et al., "Separated Detection of Ethanol and Acetone Based on SnO_2-ZnO Gas Sensor with Improved Humidity Tolerance," *Sensors and Actuators B: Chemical* 393 (2023): 134257, https://doi.org/10.1016/j.snb.2023.134257.

6. B. R. Frances, D. Balamurugan, and B. G. Jeyaprakash, "Quick Sensing Response of CuO Nanograins for Ethanol Vapour Detection: DFT Analysis of Surface Adsorption Traits," *Journal of Electronic Materials* 54 (2024): 1300–1315, https://doi.org/10.1007/s11664-024-11555-2.

7. M. Ran, Z. Yuan, H. Zhu, H. Gao, and F. Meng, "Highly Sensitive Ethanol Sensor Based on Ag NP-Modified SnO_2–$In_2Sn_2O_{7-X}$ Ternary Composite Enhanced by Synergistic Catalysis," *Materials Science in Semiconductor Processing* 170 (2024): 107967, https://doi.org/10.1016/j.mssp.2023.107967.

8. S. Zhang, P. Song, J. Sun, Y. Ding, and Q. Wang, "MoO_3/$Ti_3C_2T_X$ MXene Nanocomposites with Rapid Response for Enhanced Ethanol-Sensing at a Low Temperature," *Sensors and Actuators B: Chemical* 378 (2023): 133216, https://doi.org/10.1016/j.snb.2022.133216.

9. Z. Wu, H. Zhang, H. Ji, Z. Yuan, and F. Meng, "Novel Combined Waveform Temperature Modulation Method of NiO-In_2O_3 Based Gas Sensor for Measuring and Identifying VOC Gases," *Journal of Alloys and Compounds* 918 (2022): 165510, https://doi.org/10.1016/j.jallcom.2022.165510.

10. N. M. Pardeshi, R. S. Ghuge, P. N. Birla, et al., "Reduced Graphene Oxide/ZnO Nanocomposites: One-Step Solid-State Preparation for Room Temperature Photo-Sensing and Photoelectrical Gas Sensing Capabilities," *Nanoscale* 7 (2025): 12220–12234, https://doi.org/10.1039/D4NR04345F.

11. X. Zhao, L. Xu, Q. Chen, et al., "Highly Conductive Multifunctional rGO/CNT Hybrid Sponge for Electromagnetic Wave Shielding and Strain Sensor," *Advanced Materials Technologies* 4 (2019): 1900443, https://doi.org/10.1002/admt.201900443.

12. S. F. Tseng and C. W. Chen, "Synthesis of Nanograiny SnO_2 Films on Laser-patterned Graphene/Ceramic Substrates for Low-temperature Ethanol Gas Sensors," *Ceramics International* 47 (2021): 33498–33508, https://doi.org/10.1016/j.ceramint.2021.08.258.

13. K. Mariyappan, P. Saravanakumar, R. Thamizhselvan, P. Ragupathy, and M. Ulaganathan, "In-Situ N-rGO Scaffold @3D Graphite Felt for High Power Polyhalide Hybrid Redox Flow Battery," *Advanced Materials Technologies* 8 (2023): 2200869, https://doi.org/10.1002/admt.202200869.

14. Z. Liu, G. Xie, J. Li, H. Li, and Y. Su, "Uric Acid Sensing with Non-Enzymatic Cadmium Sulfide Decorated with rGO," *Journal of Materials Science: Materials in Electronics* 36, no. 10 (2025): 1–10.

15. X. Xu, S. Yun, G. Yang, et al., "Oxygen Vacancy-Mediated 3D/2D Hydrange-Type Bismuth Oxides with 1D Bi_2Se_3 Nanowires Confined via a Mild Selenization Strategy to Trigger Dual Built-in Electric Fields for Accelerated Energy Conversion," *Advanced Functional Materials* (2025): 2504278, https://doi.org/10.1002/adfm.202504278.

16. R. Ouyang, Y. Ma, L. Jiang, et al., "Cocatalysis of Catalytic Hairpin Assembly and Ternary Heterojunction Bi_2S_3@MoS_2@Bi_2MoO_6 Promotes Ultra-Sensitive Electrochemical of Detection MiRNA-21," *Microchimica Acta* 192 (2025): 115.

17. Y. Lou, D. Qiu, S. Chen, et al., "Integrating Bi2MoO6 Nanoflakes into TiO_2 Photoanode for Efficient Charge Separation in Photoelectrochemical Water Splitting," *Journal of Environmental Chemical Engineering* 11 (2023): 111215, https://doi.org/10.1016/j.jece.2023.111215.

18. Y. Wang, J. Li, D. Zhang, et al., "Hydrothermal Synthesis of Ag-doped WO_3-based H_2S Room Temperature Sensors: Unprecedented High and Fast Response," *Sensors and Actuators B: Chemical* 438 (2025): 137811, https://doi.org/10.1016/j.snb.2025.137811.

19. V. Paolucci, V. Ricci, D. Mastrippolito, L. Ottaviano, and C. Cantalini, "Amorphous a-Cr_2O_3 Nanosheets for NO_2 and NH_3 Gas Sensing," *ACS Applied Nano Materials* 9 (2025): 649–660, https://doi.org/10.1021/acsanm.5c04892.

20. G. Kresse and J. Furthmüller, "Efficient Iterative Schemes for *Ab Initio* Total-Energy Calculations Using a Plane-wave Basis Set," *Physical Review B* 54 (1996): 11169–11186, https://doi.org/10.1103/PhysRevB.54.11169.

21. J. P. Perdew, K. Burke, and M. Ernzerhof, "Generalized Gradient Approximation Made Simple," *Physical Review Letters* 77 (1996): 3865–3868, https://doi.org/10.1103/PhysRevLett.77.3865.

22. E. Caldeweyher, S. Ehlert, A. Hansen, et al., "A Generally Applicable Atomic-charge Dependent London Dispersion Correction," *The Journal of Chemical Physics* 150 (2019): 154122, https://doi.org/10.1063/1.5090222.

23. A. Krishnapandi, B. Muthukutty, S. M. Chen, K. T. Arul, H. J. Shiuan, and M. Selvaganapathy, "Bismuth Molybdate Incorporated Functionalized Carbon Nanofiber as an Electrocatalytic Tool for the Pinpoint Detection of Organic Pollutant in Life Samples," *Ecotoxicology and Environmental Safety* 209 (2021): 111828, https://doi.org/10.1016/j.ecoenv.2020.111828.

24. Y. Wu, J. He, Y. Liu, et al., "Construction of Bi_2MoO_6/CdS S-scheme Heterojunction for Highly Efficiency Photocatalytic Reduction of Cr(VI) under Visible Light," *Journal of Water Process Engineering* 69 (2025): 106693, https://doi.org/10.1016/j.jwpe.2024.106693.

25. S. Dong, X. Ding, T. Guo, X. Yue, X. Han, and J. Sun, "Self-assembled Hollow Sphere Shaped Bi_2WO_6/RGO Composites for Efficient Sunlight-driven Photocatalytic Degradation of Organic Pollutants," *Chemical Engineering Journal* 316 (2017): 778–789, https://doi.org/10.1016/j.cej.2017.02.017.

26. S. Liu, W. Qing, J. Zhang, et al., "Hierarchical rGO-Based Triboelectric Sensors Enable Motion Monitoring and Trajectory Tracking," *Advanced Functional Materials* 35 (2025): 2419459, https://doi.org/10.1002/adfm.202419459.

27. T. Ni, S. Wang, J. Shi, et al., "Highly Flexible and Self-Healable Zinc-Ion Hybrid Supercapacitors Based on MWCNTs-RGO Fibers," *Advanced Materials Technologies* 5 (2020): 2000268, https://doi.org/10.1002/admt.202000268.

28. Z. Chen, J. Liang, X. Xu, G. He, and H. Chen, "CdS–Bi_2MoO_6/RGO Nanocomposites for Efficient Degradation of Ciprofloxacin under Visible Light," *Journal of Materials Science* 55 (2020): 6065–6077, https://doi.org/10.1007/s10853-020-04413-z.

29. D. Panda, A. Nandi, S. K. Datta, H. Saha, and S. Majumdar, "Selective Detection of Carbon Monoxide (CO) Gas by Reduced Graphene Oxide (rGO) at Room Temperature," *RSC Advances* 6 (2016): 47337–47348, https://doi.org/10.1039/C6RA06058G.

30. S. Yuan, Y. Zhao, W. Chen, et al., "Self-Assembled 3D Hierarchical Porous Bi_2MoO_6 Microspheres toward High Capacity and Ultra-Long-Life Anode Material for Li-Ion Batteries," *ACS Applied Materials & Interfaces* 9 (2017): 42.

31. S. Shen, W. Wu, X. Yue, et al., "BiOCl-Assisted Ultralow Temperature Growth of Large-Area Monolayer $ReSe_2$ for Infrared Photodetectors Array," *Advanced Materials Technologies* 10 (2025): 2500214, https://doi.org/10.1002/admt.202500214.

32. Q. Wu, Q. Zhang, W. Li, L. Luo, and P. Du, "Tailoring of Visible Light Driven Photocatalytic Activities of Bi_2MoO_6 Flower-Like Microspheres via Synergistic Effect of Doping and Surface Plasmon Resonance," *Chemical Engineering Journal* 475 (2023): 146192, https://doi.org/10.1016/j.cej.2023.146192.

33. Y.-T. Lai, W. T. Liu, L.-C. Chung, et al., "A Facile Microwave-Assisted Method to Prepare Highly Electrosorptive Reduced Graphene Oxide/Activated Carbon Composite Electrode for Capacitive Deionization," *Advanced Materials Technologies* 4 (2019): 1900213, https://doi.org/10.1002/admt.201900213.

34. B. Wang, W. Al Abdulla, D. Wang, and X. S. Zhao, "A Three-dimensional Porous $LiFePO_4$ Cathode Material Modified with a Nitrogen-doped Graphene Aerogel for High-power Lithium Ion Batteries," *Energy & Environmental Science* 8 (2015): 869–875, https://doi.org/10.1039/C4EE03825H.

35. B. Wang, T. Ruan, Y. Chen, et al., "Graphene-based Composites for Electrochemical Energy Storage," *Energy Storage Materials* 24 (2020): 22–51, https://doi.org/10.1016/j.ensm.2019.08.004.

36. A. Dey, "Semiconductor Metal Oxide Gas Sensors: a Review," *Materials Science and Engineering: B* 229 (2018): 206–217, https://doi.org/10.1016/j.mseb.2017.12.036.

37. S. Ahmed and S. K. Sinha, "Studies on Nanomaterial-based p-type Semiconductor Gas Sensors," *Environmental Science and Pollution Research* 30 (2023): 24975–24986, https://doi.org/10.1007/s11356-022-21218-6.

38. Q. Zhang, S. Ma, W. Liu, F. Yuan, and A. Alhadi, "Significant Butanol Gas Sensor Based on Unique Bi_2MoO_6 Porous Microspheres and ZnO Nanosheets Composite Nanomaterials," *Journal of Alloys and Compounds* 911 (2022): 164877.

39. W. Li, H. T. Lu, M. S. Doblin, A. Bacic, G. W. Stevens, and K. A. Mumford, "A Solvent Loss Study for the Application of Solvent Extraction Processes in the Pharmaceutical Industry," *Chemical Engineering Science* 250 (2022): 117400, https://doi.org/10.1016/j.ces.2021.117400.

40. L. Bi, B. Fu, J. Lin, et al., "High-Performance Ag-modified ZnO Coral-Like Nanosheets for Enhanced Ethanol Gas Sensing," *Microchimica Acta* 192 (2025): 1–13, https://doi.org/10.1007/s00604-025-07013-3.

41. X. Zhang, F. Gang, and H. Wan, "Density Functional Theory Study on Spin States of $LaCoO_3$ at Room Temperature," *Chinese Journal of Chemical Physics* 27, no. 3 (2014): 274–278, https://doi.org/10.1063/1674-0068/27/03/274-278.

42. P. Recum and T. Hirsch, "Graphene-Based Chemiresistive Gas Sensors," *Nanoscale Advances* 6 (2023): 11–31, https://doi.org/10.1039/D3NA00423F.

43. N. D. Chinh, N. D. Quang, H. Lee, et al., "NO Gas Sensing Kinetics at Room Temperature under UV Light Irradiation of in_2O_3 Nanostructures," *Scientific Reports* 6, no. 1 (2016): 35066, https://doi.org/10.1038/srep35066.

44. N. Barsan and U. Weimar, "Conduction Model of Metal Oxide Gas Sensors," *Journal of Electroceramics* 7 (2001): 143–167, https://doi.org/10.1023/A:1014405811371.

45. N. Zhang, H. Zhang, J. Liu, et al., "Regulating Sodium Vacancy and Local Coordination Structure Enabled Stable Mn-Based NASICON Cathodes," *Angewandte Chemie International Edition* 138 (2026): 14839, https://doi.org/10.1002/ange.202514839.

46. T. Ruan, B. Wang, Y. Yang, et al., "Interfacial and Electronic Modulation via Localized Sulfurization for Boosting Lithium Storage Kinetics," *Advanced Materials* 32 (2020): 2000151, https://doi.org/10.1002/adma.202000151.

47. B. Wang, T. Liu, A. Liu, et al., "A Hierarchical Porous C@$LiFePO_4$/Carbon Nanotubes Microsphere Composite for High-Rate Lithium-Ion Batteries: Combined Experimental and Theoretical Study," *Advanced Energy Materials* 6 (2016): 1600426, https://doi.org/10.1002/aenm.201600426.

48. B. Wang, Y. Xie, T. Liu, et al., "$LiFePO_4$ Quantum-Dots Composite Synthesized by a General Microreactor Strategy for Ultra-High-Rate Lithium Ion Batteries," *Nano Energy* 42 (2017): 363–372, https://doi.org/10.1016/j.nanoen.2017.11.040.

49. M. Shooshtari, "Gold-decorated Vertically Aligned Carbon Nanofibers for High-Performance Room-Temperature Ethanol Sensing," *Microchimica Acta* 192 (2025): 1–13, https://doi.org/10.1007/s00604-025-07367-8.

50. W. Yan, Y. Liu, G. Shao, et al., "Chemical Surface Adsorption and Trace Detection of Alcohol Gas in Graphene Oxide-Based Acid-Etched SnO_2 Aerogels," *ACS Applied Materials & Interfaces* 13 (2021): 20467–20478, https://doi.org/10.1021/acsami.1c00302.

51. X. Duan, W. Tian, H. Zhang, et al., "Sp^2/sp^3 Framework from Diamond Nanocrystals: a Key Bridge of Carbonaceous Structure to Carbocatalysis," *ACS Catalysis* 9 (2019): 7494–7519, https://doi.org/10.1021/acscatal.9b01565.

52. J. Guo, L. Shi, J. Zhao, et al., "Enhanced Visible-light Photocatalytic Activity of Bi_2MoO_6 Nanoplates with Heterogeneous Bi_2MoO_{6-x}@Bi_2MoO_6 Core-shell Structure," *Applied Catalysis B: Environmental* 224 (2018): 692–704, https://doi.org/10.1016/j.apcatb.2017.11.030.

53. U. T. Nakate, P. Patil, Y. T. Nakate, S. I. Na, Y. T. Yu, and Y. B. Hahn, "Ultrathin Ternary Metal Oxide Bi_2MoO_6 Nanosheets for High Performance Asymmetric Supercapacitor and Gas Sensor Applications," *Applied Surface Science* 551 (2021): 149422, https://doi.org/10.1016/j.apsusc.2021.149422.

54. T. Yuan, Z. Li, W. Zhang, et al., "Highly Sensitive Ethanol Gas Sensor Based on Ultrathin Nanosheets Assembled Bi_2WO_6 with Composite Phase," *Science Bulletin* 64 (2019): 595–602, https://doi.org/10.1016/j.scib.2019.04.014.

55. S. X. Cai, X. Q. Song, Z. T. Chi, et al., "Rational Design of Bi-doped rGO/Co_3O_4 Nanohybrids for Ethanol Sensing," *Sensors and Actuators B: Chemical* 343 (2021): 130118, https://doi.org/10.1016/j.snb.2021.130118.

56. S. U. Din, M. U. Haq, R. Khatoon, et al., "A Novel Ethanol Gas Sensor Based on α-$Bi_2Mo_3O_{12}$/Co_3O_4 Nanotube-Decorated Particles," *RSC Advances* 10 (2020): 21940–21953, https://doi.org/10.1039/D0RA02591G.

57. Y. Li, N. Luo, G. Sun, et al., "In Situ Decoration of Zn_2SnO_4 Nanoparticles on Reduced Graphene Oxide for High Performance Ethanol Sensor," *Ceramics International* 44 (2018): 6836–6842, https://doi.org/10.1016/j.ceramint.2018.01.107.

58. F. Meng, Z. Yang, Z. Yuan, H. Zhang, and H. Zhu, "Hydrothermal Synthesis of CuO/rGO Nanosheets for Enhanced Gas Sensing Properties of Ethanol," *Ceramics International* 49 (2023): 5595–5603, https://doi.org/10.1016/j.ceramint.2022.10.174.

59. C. Zheng, C. Zhang, K. Zhang, et al., "Growth of $ZnFe_2O_4$ Nanosheets on Reduced Graphene Oxide with Enhanced Ethanol Sensing Properties," *Sensors and Actuators B: Chemical* 330 (2021): 129280, https://doi.org/10.1016/j.snb.2020.129280.

Supporting Information

Additional supporting information can be found online in the Supporting Information section.

Supporting File: admt71157-sup-0001-SuppMat.docx.